CFD-DEM Simulation of Superquadric Cylindrical Particles in a Spouted Bed and a Rotor Granulator

Philipp Grohn[1,*], Luca Schaedler[1], Aitor Atxutegi[2], Stefan Heinrich[2], and Sergiy Antonyuk[1]

DOI: 10.1002/cite.202200121

Dedicated to Prof. Dr.-Ing. Joachim Werther on the occasion of his 80th birthday

The fluidization behavior of cylindrical particles in a spouted bed was first investigated experimentally using a camera setup. The obtained average spouted bed height was used to evaluate the accuracy of different drag models in CFD-DEM simulations with the superquadric approach to model the particle shape. The drag model according to Sanjeevi et al. showed the best agreement. With this model, cylindrical particles were simulated in a rotor granulator and the particle dynamics were compared with the fluidization of volume equivalent spherical particles.

Keywords: CFD-DEM simulation, Fluidized bed rotor granulator, Non-spherical drag models, Spouted bed, Superquadric approach

Received: June 29, 2022; *revised:* August 28, 2022; *accepted:* October 25, 2022

1 Introduction

In the pharmaceutical industry in particular, cylindrical pellets are usually produced by extrusion and then rounded in a spheronizer, dried and coated [1]. Fluidized bed rotor granulators (FBRG), which combine all three process steps, are highly suitable for this purpose. This is achieved by the special design of a FBRG, which consists of a rotating round base plate and a fixed cylindrical wall with an annular gap for the fluidization air [2–5].

With the rapid increase in computing power, numerical simulation is becoming increasingly important for the prediction and description of complex multiphase processes, such as fluidized beds. With the two-way coupling of computational fluid dynamics (CFD) and discrete element method (DEM) it is possible to model and simulate the gas and particular phases even in complex processes. Two-way coupling CFD-DEM simulations are particularly suitable to obtain more in-depth knowledge of particle dynamics in fluidized beds [6–9]. In CFD, the flow field of the gas in the process is determined, treating the fluid phase as a continuum. In DEM, the interactions of the individual particles are calculated based on contact models describing the physical properties of the particles, such as adhesion, and their mechanical behavior under slow, fast, and repeated loading [5, 9–14]. Most CFD-DEM based studies of fluidized beds in the literature describe processes with spherical particles or non-spherical particles which are considered as spheres with an equivalent diameter. Muguruma et al. [15] were the first to numerically investigate the particle dynamics of round particles in a rotor processor without fluidizing gas using DEM. Neuwirth [16] and Grohn et al. [5] considered the fluidization gas flow and investigated the dynamics of spherical particles in a FBRG with CFD-DEM simulations.

Due to their shape, the use of ideal spheres leads to fast detection of solid contact, since the surface of a sphere always has the same distance to its center. However, many products and particular materials are mostly of irregular shape. Simplifying real particle shapes to spheres is useful when particles only present slight irregularities, or when their size is small enough to assume that the shape is irrelevant compared to other factors such as solid viscosity or capillarity [17]. Some authors [18, 19] slightly increased the DEM friction parameters to implicitly account for shape irregularities. However, Govender et al. [19] found that the spherical description sometimes cannot properly represent the rolling of particles, the deviation of porosity, and the segregation of particle mixtures with highly irregularly shaped particles.

[1]Philipp Grohn https://orcid.org/0000-0003-3111-672X,
Luca Schaedler, Prof. Sergiy Antonyuk
(Philipp.grohn@mv.uni-kl.de)
Technische Universität Kaiserslautern, Institute of Particle Process Engineering, Gottlieb-Daimler-Straße 44, 67663 Kaiserslautern, Germany.

[2]Aitor Atxutegi, Prof. Stefan Heinrich
Hamburg University of Technology, Institute of Solids Process Engineering and Particle Technology, Denickestraße 15 (K), 21073 Hamburg, Germany.

There are different methods to consider the particle shape in numerical simulations [20]. A common approach is to use the multisphere model according to Favier et al. [21]. A cluster of overlapping spheres that do not interact with each other is used for the shape representation of the particles. From the sum of the force balances on each sphere, the dynamics of the entire cluster can be calculated. Depending on the complexity of the particle shape and the accuracy of the mapping, the number of individual spheres in the cluster varies [22]. The increasing number of spheres per cluster leads to a direct increase in the time required for the contact detection, and thus in the computational time of a simulation [6, 22–26]. A disadvantage of this method is that the internal stresses of the multisphere particle are inadequately mapped and the deformation properties also depend on the number of individual spheres in the cluster. Using the multisphere approach, Weis et al. [13, 27] studied the particle dynamics of cylinders during the particle rounding in a spheronizer, which is similar to processes inside a FBRG.

Another approach to consider the particle shape of solids such as cylinders, cubes, ellipsoids, and rhomboids is given by the superquadric (SQ) expression. For these shapes, it is a more direct and computationally efficient approach. A superquadric shape is described by the parameterized equation proposed by Barr et al. [28]. The superquadric approach offers the advantage that only one centroid and one orientation are needed to track the particle. Cleary [29] used this approach to simulate the mixing properties of non-spherical particles in DEM. He found that the mixing process is less effective for elongated particles than for spherical ones. Also in DEM, Ma et al. [30, 31] analyzed the effect of the aspect ratio of ellipsoidal and rod-shaped particles on diffusion and convection based on the orientation distribution of particles. Ji et al. [32] used DEM simulations to investigate the mixing process of spherical and non-spherical particles in a horizontal rotating drum with a good agreement between the experimental and simulated values. Often, flat spouted bed apparatuses are used to validate CFD-DEM simulations, because the pseudo 2D motion of the particles in the bed can be well obtained with particle image velocimetry (PIV). This method was used in our previous work experimentally only [33] as well as experimentally and numerically [11, 12]. Atxutegi et al. [6] implemented different drag models for superquadric particles in CFD-DEM. They calculated the particle motion of spherical and ellipsoidal particles in a spouted bed using different drag models and compared the results with experimental measurements. For the ellipsoidal particles, the drag model of Sanjeevi et al. [34] was found to be the most suitable. Gao et al. [35] investigated the fluidization behavior of cylinders, rods, and cuboid particles in a fluidized bed using CFD-DEM and implemented two different drag models. The comparison of the simulation results with the experimental measurements showed the best agreement with the drag model according to Hölzer and Sommerfeld [36]. It was found that the deviation of the fluidized bed height was between 10 % and 14 %.

The aim of this study is to investigate the influence of the particle shape modeled with the superquadric approach on the dynamics of spherical and cylindrical particles in a FBRG using CFD-DEM simulations. First, the fluidization behavior of cylindrical particles in a spouted bed is calculated using four different drag models in CFD-DEM simulations. The numerical results are validated with experimental data of the spouted bed height. Subsequently, the most suitable drag model is used to simulate the particle motion of such cylindrical particles in a FBRG. Then, the results for the cylindrical particles are compared with those for volumetric equivalent spherical particles to draw conclusion about the influence of particle shape.

2 Model Description

2.1 CFD-DEM Model

For the simulations, the CFD was coupled with the DEM. For this purpose, CFD describes the fluid phase by the volume-averaged Navier-Stokes equation considering the volume fraction of the gas phase ε_g and the momentum sink term $\vec{S}_p$ of the particulate phase. The equation is solved in the Eulerian framework with a finite volume method. The mass and momentum governing equations are [37]:

$$\frac{\partial\left(\varepsilon_g\rho_g\right)}{\partial t}+\nabla\left(\varepsilon_g\rho_g\vec{u}_g\right)=0 \tag{1}$$

$$\frac{\partial\left(\varepsilon_g\rho_g\vec{u}_g\right)}{\partial t}+\nabla\left(\varepsilon_g\rho_g\vec{u}_g\vec{u}_g\right)=-\varepsilon_g\nabla p+\nabla\left(\varepsilon_g\vec{\tau}_g\right)+\vec{S}_p+\varepsilon_g\rho_g\vec{g} \tag{2}$$

where ρ_g is the density, p represents the pressure, $\vec{u}_g$ describes the velocity and τ_g is the stress tensor of the gas phase. The particulate phase is determined in DEM, firstly introduced by Cundall and Strack [38], where the motion of each single particles is calculated by the motion equations for translation and rotation according to Newton and Euler. To account for the influence of the gas phase on the particles, the drag force $\vec{F}_{D,i}$, pressure gradient force $\vec{F}_{\nabla p,i}$ and viscous gas force $\vec{F}_{\vec{\tau},i}$ are additionally considered:

$$m_{p,i}\frac{d\vec{v}_{p,i}}{dt}=\vec{F}_{D,i}+\vec{F}_{\nabla p,i}+\vec{F}_{\vec{\tau},i}+\vec{F}_{g,i}+\sum_{j=0}^{k}\vec{F}_{c,ij} \tag{3}$$

$$I_{p,i}\frac{d\vec{\omega}_{p,i}}{dt}=\sum_{j=0}^{k}\left(\vec{M}_{t,ij}+\vec{M}_{r,ij}\right) \tag{4}$$

where $\vec{v}_{p,i}$ describes the translational velocity of each particle with the mass $m_{p,i}$, $\vec{F}_{g,i}$ is the gravitational force and the sum of $\vec{F}_{c,ij}$ represents all contact forces acting on the

particle due to interactions with other particles or walls. For the calculation of the angular velocity $\vec{\omega}_{p,i}$ of each particle with the moment of inertia $I_{p,i}$, the sums of the torques $\vec{M}_{t,ij}$ caused by the tangential forces acting on the particle and the sum of the torques $\vec{M}_{r,ij}$ due to rolling friction are determined. A more detailed description of the CFD-DEM coupling can be found in [7, 39, 40].

2.2 Superquadric Approach

The superquadric approach is a general method of mathematically describing the particle shapes of non-spherical particles with five degrees of freedom. It allows the modeling of a large variety of particle shapes used in industry [23, 28, 41]. The superquadric equation is given as [28]:

$$\left(\left|\frac{x}{r_x}\right|^{n_2}+\left|\frac{y}{r_y}\right|^{n_2}\right)^{n_1/n_2}+\left|\frac{z}{r_z}\right|^{n_1}=1 \tag{5}$$

where r_x, r_y, r_z are the semi-axis lengths of the superquadric elements, n_1 and n_2 are blockiness parameters that control edge sharpness and x, y, and z are the coordinates of the center of gravity. An ellipsoid for example results in $n_1 = n_2 = 2$, a cylinder-shaped element is obtained if $n_1 \gg 2$ and $n_2 = 2$, and a cubic shape is generated if $n_1 = n_2 \gg 2$.

The detection of particle contacts requires only the solution of one set of nonlinear equations per particle. In the used DEM framework the equations are solved by Newton-Raphson iterative routine which is well described by Verbeke and Cools [42]. The whole algorithm for contact detection was developed by Podlozhnyuk et al. [40]. They extended the soft-spherical approach for non-spherical particles:

$$F_{c,ij,n} = -k_{n,ij}\delta_{n,ij} - \eta_n u_{n,ij} \tag{6}$$

$$F_{c,ij,t} = \begin{cases} -k_{t,ij}\delta_{t,ij} - \eta_t u_{t,ij} & \text{if } \left|F_{c,ij,t}\right| \le \mu\left|F_{c,ij,n}\right| \\ -\mu\left|F_{n,ij}\right| & \text{if } \left|F_{c,ij,t}\right| > \mu\left|F_{c,ij,n}\right| \end{cases} \tag{7}$$

where $\delta_{n,ij}$ and $\delta_{t,ij}$ are the normal and tangential displacement, $u_{n,ij}$ and $u_{t,ij}$ are the normal and tangential component of the contact velocity vector of the particle with another particle or a wall and μ is the sliding friction coefficient. η_n and η_t are the normal and tangential damping coefficients, respectively. The spring stiffness and damping coefficient were calculated using the Hertz-Tsuji model [43] and a modified equivalent radius as proposed by Podlozhnyuk et al. [40]. They calculated the contact force of colliding superquadric particles using the mean local curvature coefficient [44] of the contact point. A detailed description of the superquadric approach used in this work is given by Podlozhnyuk et al. [40].

2.3 Drag Force Modeling

The drag force acting on the particle is determined by the following equation:

$$\vec{F}_{D,i} = \frac{1}{8} C_D \rho_g \pi d_p^2 \left(\vec{u}_g - \vec{u}_p\right)\left|\vec{u}_g - \vec{u}_p\right| \varepsilon_g^{2-\beta} \tag{8}$$

where $\left(\vec{u}_g - \vec{u}_p\right)$ describes the relative velocity of a particle and the gas phase and C_D is the drag coefficient. The drag forces for spherical particles are calculated in this study according to the well-known drag model proposed by Di Felice [45]. In recent years, several models have been developed to calculate the drag force of non-spherical particles. Extensive work in this field was done by Atxutegi et al. [6], who implemented a total of four correlations of the drag coefficient for non-spherical particles modeled with the superquadric approach. The implemented code was also used in this study. An overview of the compared drag coefficient models can be seen in Tab. 1.

The often used correlation of Hölzer and Sommerfeld [36] (Eq. (9)) considers the shape and fluid-solid relative orientation based on the surfaces projected on the streamwise and crosswise planes. There is no limitation for the application of this correlation in terms of shape and Reynold number. Based on Lattice Boltzmann method, Sanjeevi et al. [34] proposed a drag model (Eqs. (13) and (14)). They followed the expression developed by Zastawny et al. [48] in which a_i are fitting parameters corresponding to the particle shape. The last two correlations for the drag force (Eqs. (15) and (21)) are similar in structure. Dioguardi et al. [47] improved the model proposed by Bagheri and Bonadonna [46]. In both models, the factor of particle shape is taken into account. Dioguardi et al. [47] also requires an iterative calculation of the final particle velocity.

In Fig. 1, the drag coefficients versus the particle Reynolds number are plotted for a spherical particle according to Di Felice's drag model [45] and for an equal-volume cylindrical particle according to the four drag models implemented. While the model of Bagheri and Bonadonna [46] always gives lower drag coefficients than Di Felice [45], the drag coefficients according to the model of Dioguardi et al. [47] are slightly higher. As described, the drag force models of Hölzer and Sommerfeld [36] and Sanjeevi et al. [34] depend on the angle of attack (angle between the particle central axis of symmetry and the orientation of the incident fluid). Both models estimate different drag coefficients depending on the particle orientation, with C_D being higher if the cylindrical particle biggest surface area is normal to the fluid flow. The drag coefficients for both models for 0° are always below Di Felice [45], but for 90° they are clearly above. Further information can be found in Atxutegi et al. [6].

Table 1. Correlations for the drag coefficient for superquadric particles.

Model	Equations	
Hölzer and Sommerfeld [36]	$c_D = \frac{8}{Re_p\sqrt{\Phi_\parallel}} + \frac{16}{Re_p\sqrt{\Phi}} + \frac{3}{\sqrt{Re_p}\Phi^{3/4}} + 0.421\times 10^{0.4(-\log\Phi)^{0.2}}\frac{1}{\Phi_\perp}$	(9)
	$\Phi = \frac{\pi d_{eq}^2}{\frac{8r_xr_yr_z}{n_1n_2}B\left(\frac{1}{n_1},\frac{2}{n_1}+1\right)B\left(\frac{1}{n_2},\frac{1}{n_2}+1\right)}$	(10)
	$\Phi_\perp = \frac{\pi d_{eq}^2}{4\Psi_\perp}$	(11)
	$\Phi_\parallel = \frac{\pi d_{eq}^2}{4\left(\frac{84r_yr_z}{n_1n_2}B\left(\frac{1}{n_1},\frac{2}{n_1}+1\right)B\left(\frac{1}{n_2},\frac{1}{n_2}+1\right)-\Psi_\parallel\right)}$	(12)
Sanjeevi et al. [34]	$c_{D,\sigma} = c_{D,\sigma=0^\circ} + \left(c_{D,\sigma=90^\circ} - c_{D,\sigma=0^\circ}\right)\sin^2\sigma$	(13)
	$c_{D,0^\circ,90^\circ} = \left(\frac{a_1}{Re_p} + \frac{a_2}{Re_p^{a_3}}\right)e^{-a_4Re_p} + a_5\left(1-e^{-a_4Re_p}\right)$	(14)
Bagheri et al. [46]	$c_D = \frac{24\kappa_S}{Re_p}\left[1+0.125\left(Re_p\kappa_N/\kappa_S\right)^{2/3}\right] + \frac{0.46\kappa_N}{1+\frac{5330}{Re_p\kappa_N/\kappa_S}}$	(15)
	$\kappa_S = \left(F_S^{1/3} + F_S^{-1/3}\right)/2$	(16)
	$\kappa_N = 10^{\alpha_2[-\log F_N]^{\beta_2}}$	
	$\alpha_2 = 0.45 + 10/\left(e^{(2.5\log\rho')}+30\right)$	(17)
	$\beta_2 = 1 - 37/\left(e^{(3\log\rho')}+100\right)$	(18)
	$F_S = fe^{1.3}\left(d_{eq}/LIS\right) = d_{eq}^3/\left(L^{2.3}I^{0.7}\right)$	(19)
	$F_N = f^2e\left(d_{eq}^3/LIS\right) = d_{eq}^3S/\left(L^2I^2\right)$	(20)
Dioguardi et al. [47]	$c_D = \frac{24}{Re_t}\left(\frac{1-\Psi}{2}+1\right)^{0.25} + \frac{24}{Re_t}\left(0.1806\,Re_t^{0.6459}\right)\Psi^{-Re_t^{0.08}} + \frac{0.4251}{1+\frac{6880.95}{Re_t}\Psi^{5.05}}$	(21)

3 Validation of the Drag Models

3.1 Setup of the Spouted Bed and Simulation Parameters

In order to validate the drag models (Tab. 1) with the superquadric approach and to select the most appropriate model for the prediction of the drag force acting on cylindrical particles during fluidization, the experiments in a spouted bed apparatus (Fig. 2a) were performed. The walls of the prismatic spouted bed setup were constructed from transparent polymethyl methacrylate and the bottom consisted of a wire mesh with a 3 mm × 3 mm mesh width and 0.8 mm thick wire. The fluidization of the particles was recorded with a HD camera (a2A2590-60ucPRO, Basler AG) at 60 Hz. A LED light (Constellation 120E, Integrated Design Tools Inc.) provided good exposure. A pressure gauge (MULTIFIX Druckregler 0,5–10 bar, RIEGLER & Co. KG) and rotameter (L16/630, Rota Apparate- und Maschinenbau Dr. Hennig GmbH & Co. KG) were used to set the

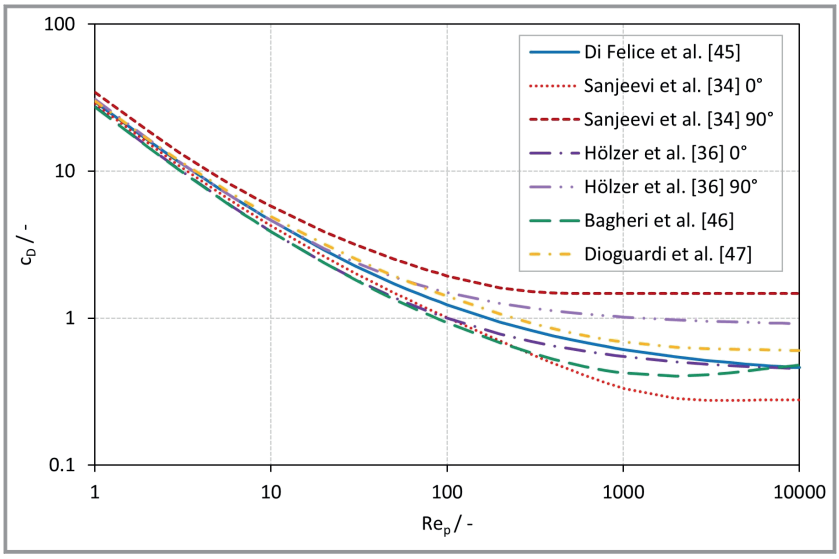

Figure 1. Evolution of the drag coefficient as a function of the Re number for each drag model.

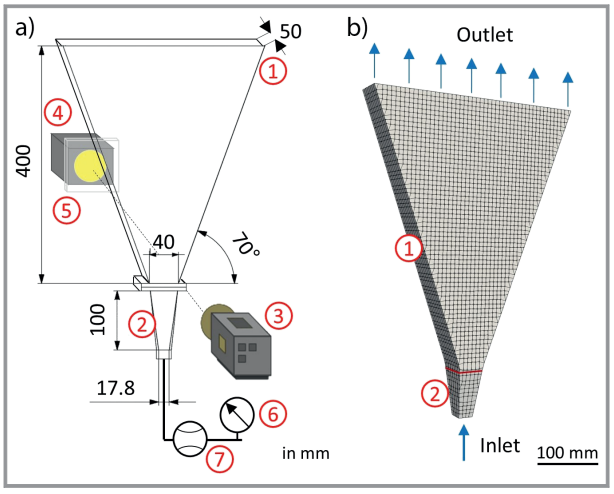

Figure 2. a) Experimental setup of the spouted bed and b) discretized spouted bed for the simulations consisting of 1) process chamber, 2) gas inlet channel, 3) HD camera, 4) LED light, 5) diffusing plate, 6) manometer and 7) rotameter.

volume flow. Several grounding cables on the equipment provided discharge of the minor electrostatic effects during the fluidization experiments.

The geometry of the spouted bed was discretized with snappyHexMesh (Fig. 2b) consisting of 13 712 cells. The CFD-DEM coupling was carried out using the software CFDEMcoupling [39]. The gas flow field was solved with OpenFOAM (OpenFoam v6). Ambient air with a density of 1.2 kg m^{-3} was considered as an incompressible fluid in all simulations. The k–ε model [49] was used to account for turbulence. The CFD parameters are listed in Tab. 2.

The discrete phase was solved with DEM using the software LIGGGHTS [39]. Cylindrical particles made of beech wood were taken in the experiments and considered in the simulations. According to Wen and Yu [50], the minimum fluidization velocity of spheres of equal volume was about 0.91 m s^{-1}. Similar to our previous works [5, 51], we used different experimental setups to obtain the particle properties needed for the contact model in DEM. In order to determine the Young's modulus and the coefficient of restitution, a Nanoindenter (Hysitron TI Premier, Bruker Corporation) was used. The static and rolling friction coefficients were obtained with a Texture Analyser® (TA.XTplus, Stable Micro Systems). Tab. 3 presents the particle properties for the DEM simulations.

Table 2. Parameters for the CFD simulation of the spouted bed.

Parameters of the gas	Unit	Value
Number of grid cells	–	13 712
CFD time step	s	2×10^{-5}
Gas	–	Air
Turbulence model	–	k–ε
Kinematic viscosity	m^{2}s^{-1}	1.58×10^{-5}
Gas temperature	°C	20
Gas density	kg m^{-3}	1.2

Table 3. Parameters for the DEM simulation of the spouted bed.

Parameters of the particles	Unit	Value
Bed mass	G	70
Number of particles	–	1465
Density	kg m^{-3}	730
Young's modulus	GPa	12
Poisson's ratio	–	0.3
Static friction coefficient	–	0.41
Rolling friction coefficient	–	0.09
Restitution coefficient	–	0.56
Semi-axes cylinder r_x, r_y, r_z	mm	2.0, 2.0, 2.6
Blockiness n_1, n_2	–	8; 2
Time step cylinder	s	4×10^{-7}

3.2 Data Processing Method

In order to calculate the maximum average spouted bed height, the spouting is recorded in the experiment for 4 s. Using the image processing toolbox in MATLAB, a program was developed to determine the position of the 10 highest particles in each image. In the simulations, 5 s of real time are calculated. In this timeframe, the steady state from 1 s to 5 s is evaluated every 10 ms, which correspond to a total of 400 snapshots. The obtained heights of the highest particles in each snapshots were then averaged.

3.3 Comparison of the Experimental and Simulation Results

For the investigation of the maximum average spouted bed height, the gas inlet velocity is varied three times (1.36 m s^{-1}, 1.44 m s^{-1}, and 1.61 m s^{-1}). Fig. 3 shows the particle fluidization behavior for a gas inlet velocity of 1.44 m s^{-1} at three different times in the experiment and in the four simulation cases with different drag models described in Sect. 2.3. There are clear differences in the simulated fluidization of the particles. The drag models according to Sanjeevi et al. [34] and Hölzer and Sommerfeld. [36] lead to a clear formation of a fountain. The maximal bed height is achieved in the simulation with the model of Sanjeevi et al. [34]. In contrast, the use of drag models according to Bagheri et al. [46] and Dioguardi et al. [47] lead only to a poor spouting behavior.

In Fig. 4a, all averaged spouted bed heights of the particles at a gas inlet velocity of 1.44 m s^{-1} are shown over time. The highest averaged spouted bed height of the particles with the smallest fluctuations is achieved in the experiment, and with the drag relation according to Sanjeevi et al. [34]. While the model of Sanjeevi et al. [34] can reproduce the experiment well, larger fluctuations than in the experiment can be seen. The spouted bed height has the smallest fluctuations with the drag model according to Hölzer and Sommerfeld [36] but the influence of the drag force is underestimated. As previously shown in Fig. 3, the results of the models according to Bagheri et al. [46] and Dioguardi et al. [47] are very close to each other and lead to a significantly reduced fluidization of the particles. These deviations were also found for the two other investigated gas inlet velocities (Fig. 4b). For all gas inlet velocities, the drag model according to Sanjeevi et al. [34] shows the smallest deviations of on average 8.7 % from the experimental data, which are within the standard deviation of the simulation results. The spouted bed height of the particles predicted using the model of Hölzer and Sommerfeld [36] is significantly lower by 22.6 % than the experimental values. As already described, the drag models according to Bagheri et al. [46] and Dioguardi et al. [47] are not suitable to simulate the cylindrical particles in the spouted bed, because of the high underestimation of the spouted bed heights (up to 47.7 %) from the experiments. The performed study showed that the correlation of Sanjeevi et al. [1] is the best drag model to describe the fluidization of the cylindrical particles.

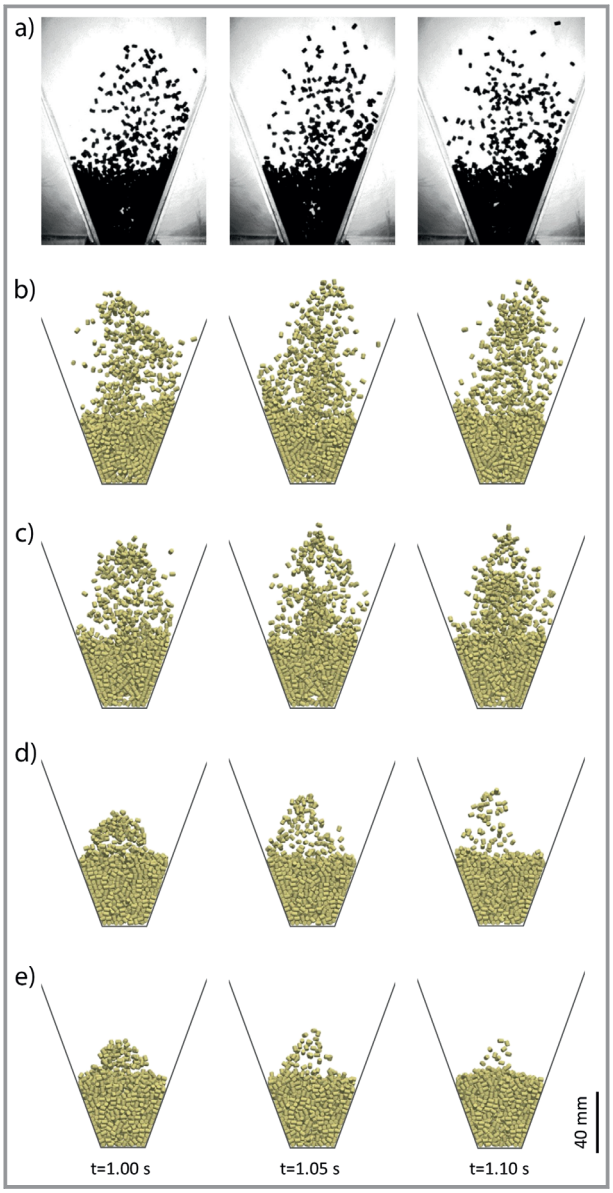

Figure 3. Snap shots of the fluidization of the cylindrical particles for a gas inlet velocity of 1.44 m s^{-1} in a) the experiment and the simulations with the drag model according to b) Sanjeevi et al. [34], c) Hölzer and Sommerfeld [36], d) Bagheri et al. [46], e) Dioguardi et al. [47].

4 Fluidized Bed Rotor Granulator

4.1 Geometry of the Fluidized Bed Rotor Granulator

The simulated apparatus in this study is a FBRG inspired by the commercially used rotary granulator Rotor 300

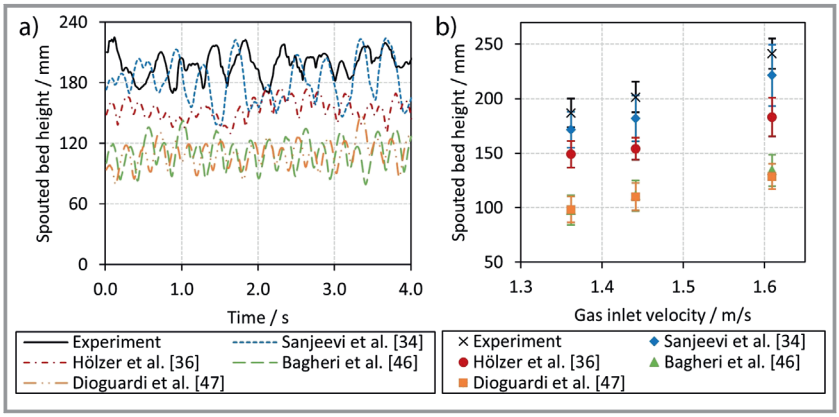

Figure 4. a) The averaged spouted bed height over time at gas inlet velocity of 1.44 m s^{-1} in the experiment and the simulations and b) the averaged spouted bed height at different gas inlet velocities obtained with experiments and the simulations.

(Glatt GmbH, Germany) with an inner diameter of 295 mm, as shown in Fig. 5. An unstructured rotating plate with a diameter of 268 mm is located in the center. From the bottom, incoming air flows through the 2 mm annular gap between the rotor plate and the apparatus wall. The high gas velocities in the gap caused by the small inflow area compared to other fluidized beds ensure the fluidization of the particle bed.

4.2 Simulation Parameters of the Fluidized Bed Rotor Granulator

Similar to our previous work [5], the geometry of the rotor granulator FBRG was discretized with HyperMesh into 99 171 cells. The same software packages as for the spouted bed in the previous section were used. The study was performed at an inlet velocity of 1.5 m s^{-1}, which resulted in a 25 times higher velocity than the minimal fluidization velocity in the gap. The rotor plate rotated at 300 rpm. Again, incompressible air with a density of 1.2 kg m^{-3} was considered in the simulation, while the turbulence was calculated according to the k-ε model. The CFD parameters are listed in Tab. 4.

In order to compare the simulation results with future experiments with a magnetic particle tracking system [52], spherical and cylindrical particles with a ceramic core and a shell of polyvinyl butyral were considered in these simulations. The particles were generated above the rotation plate. The drag force on the spherical particles was again calculated according to the Di Felice model [45], whereas for the cylindrical particles the model of Sanjeevi et al. [34] was used. The properties of the volumetric equal spherical and cylindrical particles (Tab. 5) were measured similarly to Sect. 3.1.

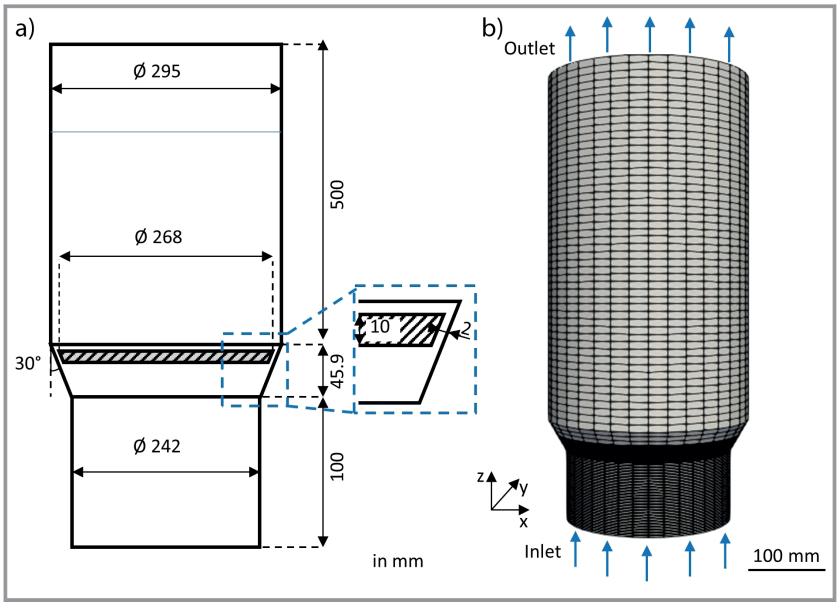

Figure 5. a) Geometry of the simulated fluidized bed rotor granulator and b) discretized fluidized bed rotor granulator.

4.3 Results

4.3.1 Particle Concentration

In order to investigate the influence of the particle shape on the bed expansion in the FBRG, the analysis of the solid volume fraction inside the apparatus is analyzed. For the determination of the solid volume fraction, the inner volume of the apparatus was discretized into 3 mm × 3 mm squares in axial and radial directions. The volume of particles located within this regular poloidal discretization grid was calculated and averaged every 10 ms during the steady-state periods of the simulations and divided by the volume of the associated ring cell. The same procedure can be found in Weis et al. [2]. The obtained data were then averaged over the whole analyzed time period. The calculated solid volume fractions for the spherical and cylindrical particles are shown in Fig. 6. A clear difference can be observed between the two cases. The particle bed of the spherical particles is much denser than in the case of the cylindrical particles. While the spheres move along the wall up to a maximum height of 40 mm above the

Table 4. Parameters for the CFD simulation of the fluidized bed rotor granulator.

Parameters of the gas	Unit	Value
Number of grid cells	–	99 171
Time	–	steady
Turbulence model	–	k–ε
Inlet velocity	$m\,s^{-1}$	1.5
Temperature	°C	20
Time step sphere	s	5×10^{-5}
Time step cylinder	s	2×10^{-5}
Kinematic viscosity	m^2s^{-1}	1.58×10^{-5}
Gas density	$kg\,m^{-3}$	1.2

Table 5. Parameters for the DEM simulation of the fluidized bed rotor granulator.

Parameters of the particles	Unit	Value
Diameter sphere	mm	4.02
Semi-axes cylinder r_x, r_y, r_z	mm	1.5, 1.5, 2.5
Blockiness n_1; n_2	–	8; 2
Bed mass	kg	1.0
Number of particles	–	4626
Density	$kg\,m^{-3}$	6370
Young's modulus	GPa	15.5
Poisson's ratio	–	0.3
Static friction coefficient	–	0.28
Rolling friction coefficient	–	0.07
Restitution coefficient	–	0.51
Time step sphere	s	5×10^{-7}
Time step cylinder	s	4×10^{-7}
Rotation of the plate	rpm	300

rotating plate, the cylindrical particles fly up to a maximum height of 80 mm. The bed is also wider in the radial direction for the cylindrical particles with a lower particle density than for spheres. In the bed zone just above the rotor plate, the curvature of the bed surface changes from convex to concave for cylinders. It can also be observed that at the top of the bed the spherical particles form a region with constant height of the horizontal bed surface. This is not the case with cylinders, where the bed surface is convex. Overall, the particle bed expands more than 3.5 times wider in the case of the cylindrical particles than in the case of the spherical ones. This can be explained by the fact that the drag coefficient for the cylindrical particles is up to 3.3 times higher than for the spheres. In both cases, there is a region of high concentration near the wall in the upper part of the particle bed. In this zone, the motion direction of the particles flying upwards is reversed. Furthermore, for cylinders, a zone of high concentration can be seen around the gap between the rotor plate and the wall. For spheres, the solid volume fraction decreases here.

4.3.2 Particle Velocity

The absolute velocity distribution of the spherical and cylindrical particles can be seen in Fig. 7. The velocity distribution of the spherical particles is trimodal (peak at $0.55\,m\,s^{-1}$), whereas it is bimodal for the cylinders (peak at $0.37\,m\,s^{-1}$). The average particle velocities also differs, whereby with an average velocity of $0.62\,m\,s^{-1}$, the cylinders are 15.8 % slower than the spherical particles with $0.74\,m\,s^{-1}$. In general, the distribution of particle velocities is much broader in the case of cylindrical particles.

In order to take a more detailed look at the velocity components of the absolute particle velocity, in Fig. 8 the heatmaps for the tangential velocity distribution depending on the radial and axial position of the particles are shown for both cases. Similar to the results of the solid volume fraction, for the upcoming Figs. 8–10 the inner volume of the apparatus was discretized in axial and radial directions into 3 mm × 3 mm squares. Both the spherical and the cylindrical particles have the highest tangential velocity directly above the plate. However, the particles move only at a maximum of 29 % of the maximum rotational velocity of the rotor plate. In both cases, the phenomenon of high slip can be

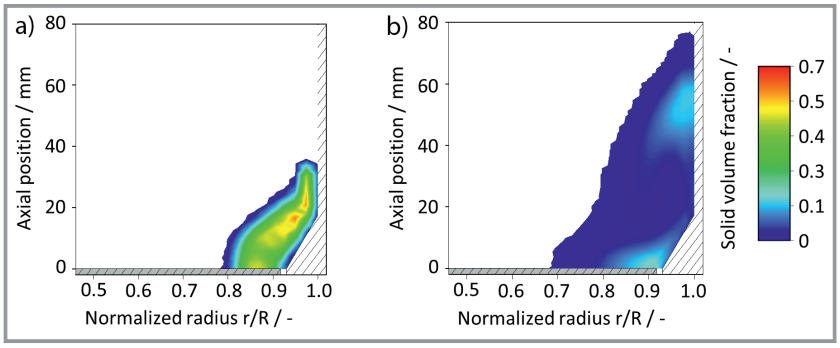

Figure 6. The time-averaged particle number density for a) the spherical particles and b) the cylindrical particles with the same volume equivalent diameter.

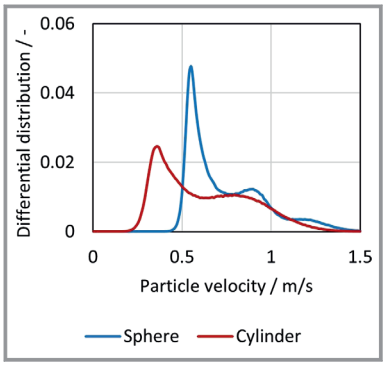

Figure 7. Distributions of the absolute velocities of spherical and cylindrical particles in the rotor granulator.

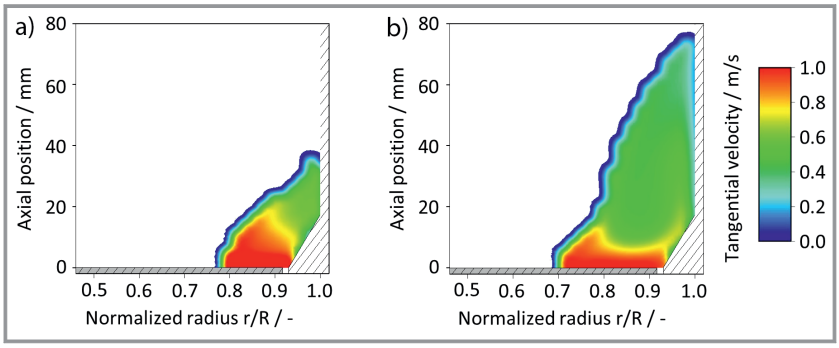

Figure 8. The tangential velocities in poloidal plot of the fluidized bed rotor granulator with a) the spherical particles and b) cylindrical particles.

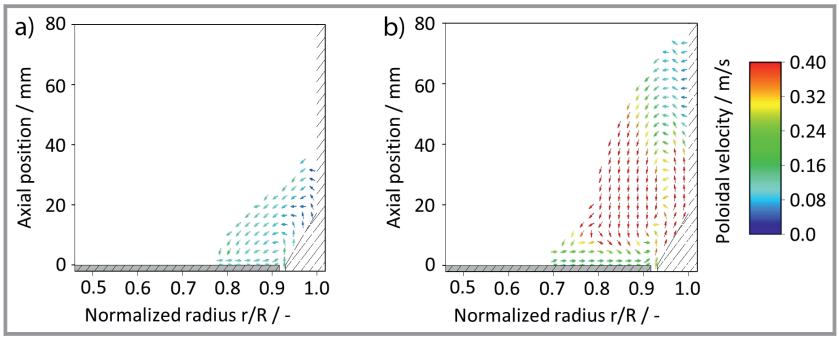

Figure 9. The poloidal velocity of a) the spherical particles and b) cylindrical particles.

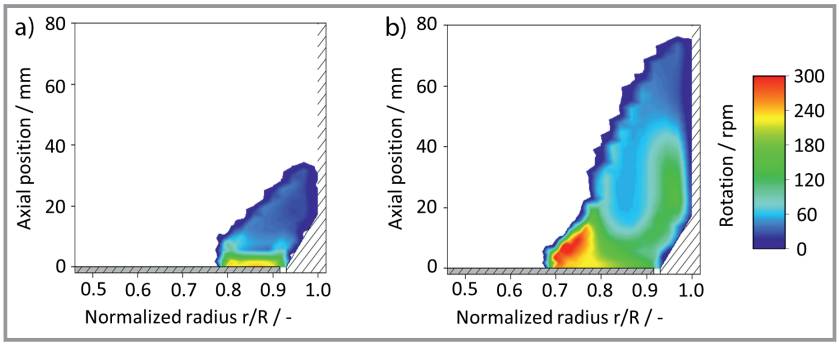

Figure 10. The rotational velocity of a) the spherical particles and b) cylindrical particles.

explained by the fact that the rotor plate is not structured and has a smooth surface. In the case of the spheres, higher tangential velocities can still be seen at bed heights of up to 20 mm, whereas the cylinders are slower from a height of 10 mm. The higher the particles move in the system, the lower their tangential velocities. Since the cylindrical particles rise much higher, the bed expansion is larger and the zone in which the particles have a low tangential velocity is also increased.

For better understanding of the particle dynamics in the bed, the poloidal velocity arrow plots of both cases are presented in Fig. 9. The poloidal velocity is the velocity component consisting of the *z*-velocity and the radial velocity. The direction of the particle movement in the poloidal plane can be seen by the velocity vectors. The spherical and the cylindrical particles move in a circular pattern in the poloidal section of the particle bed. Similar particle dynamics were also found by Weis et al. [1] during a spheronization process. However, due to the fluidization gas in the FBRG the highest poloidal velocities can be seen near the wall where the particles are vertically accelerated by the fluidization gas and in the descending zone where the particles move downwards. The cylindrical particles exhibit a much stronger acceleration in z direction above the gap and move along the conical and cylindrical parts of the wall with significantly higher velocities. Due to the two times higher bed height and the lower particle bed density in the bed, the cylindrical particles also reach a higher axial velocity than the spheres during their vertical motion. An effective possibility to describe the particle dynamics in the poloidal plane is provided by the value of the radial movement proportion (RMP) developed in our previous work [53]. RMP describes the proportion of the radial velocity to the total velocity in xy-plane of the particles. The higher this value, the more the kinetic energy of the particles goes into the radial motion of the particles in the bed. The cylindrical particles have RMP of 14.8, which is significantly higher than the value for spherical particles (RMP = 3.87). It can be concluded that the cylinders in the particle bed move with a much higher velocity in a circle in the poloidal plane than the spheres.

4.3.3 Particle Rotation

The modolus of the rotation of the particles around their center of mass is another important kinematic parameter to analyze the particle dynamic in the FBRG. The heat maps of the rotational velocity for the spherical and cylindrical particles are shown in Fig. 10. Similar to the results of the tangential and poloidal velocity of the particles, important differences between the spheres and cylinders can be seen. In general, particles in the vicinity of the rotor plate have the highest rotational velocities, which is caused by the contacts with the rotor plate. However, the cylindrical particles achieve a much higher rotational velocity than the spherical particles. In the region of the air inlet, high rotational velocities of the cylindrical particles up to 140 rpm can still be seen even at a height of more than 40 mm. With further increasing axial position, the rotational velocity is reduced. In the case of the spheres, a clear decrease in rotational velocity can already be observed from a height of 10 mm. The reason for the higher rotational velocity of the cylinders is the greater bed expansion. As a result, the free path length until a new particle contact occurs is longer and also the time period in which the particle can rotate increases. Therefore, the average rotational velocity of the cylinders is about 22 % higher than that of the spherical particles due to the higher bed porosity. In the upper reversal point of the direction of motion, the lowest rotational velocity can be seen in both cases.

5 Conclusions

In this work the fluidization behavior of cylindrical particles in a spouted bed and a fluidized bed rotor granulator were analyzed with CFD-DEM simulations using the superquadric approach for modeling of the particle shape. Firstly, the accuracy of four different drag models developed for non-spherical particles in CFD-DEM simulations was investigated by comparing the fluidization behavior of cylindrical particles in a spouted bed. Significant differences were found in the results obtained with the different drag models. To validate the simulation results, the average maximum spouted bed height was determined in experiments and the drag model according to Sanjeevi et al. [34] showed the smallest differences with a 8.7 % deviation.

This drag model was then used to study the influence of particle shape on the particle dynamics in a fluidized bed rotor granulator. Due to their shape, the intensity of the fluidization is much higher for the cylindrical particles than for the spheres of the same volume and mass. As a result, the bed porosity is higher, since the bed expands more than 3.5 times in the case of the cylindrical particles. The highest tangential velocity of particles can be seen directly above the rotor plate in both cases. As the distance from the rotor plate increases, the tangential velocity decreases and the bed slip to the rotor plate intensifies. In the poloidal plane, a clear circular motion of the particles can be seen with highest poloidal velocities near the wall where the particles are vertically accelerated by the fluidization gas and in the descending zone. Due to the lower bed density in the case of cylindrical particles, they can move more freely and reach higher axial velocities. The rotation velocity also increases due to the lower bed density and the shape for the cylinders. The highest average rotational velocities occur above the plate where the particles move downwards from top of the bed and in the area near the wall. It can be concluded that the significantly higher drag coefficient of the cylinders causes this significant difference.

This study was conducted within the research project, which is funded by the Deutsche Forschungsgemeinschaft (DFG, German Research Foundation), Project-ID–AN 782/12-1 and HE 4526/25-1, which the authors gratefully acknowledge. Open access funding enabled and organized by Projekt DEAL.

Symbols used

a_{1-5}	[–]	Sanjeevi fitting coefficients for the drag force
B	[–]	Syamlal B coefficient
C_D	[–]	Widerstandskoeffizient
e	[–]	elongation shape value
f	[–]	flatness shape value
F	[N]	force
F_g	[N]	gravitational force
F_N	[–]	Newton shape descriptor
F_S	[–]	Stokes form factor
$F\tau$	[N]	viscous gas force
I	[kg m^2]	moment of inertia
k	[kg m^{-2}]	spring coefficient
LIS	[m]	longest, intermediate, shortest particle length
M	[Nm]	torque
m	[kg]	mass
n_1, n_2	[–]	superquadric blockiness coefficient
p	[Pa]	pressure
r_x, r_y, r_z	[m]	superquadric shape value (semi-axis length)
Re	[–]	Reynolds number
S	[–]	momentum sink term
t	[s]	time
u	[ms^{-1}]	velocity
x, y, z	[–]	coordinates of center of gravity

Greek letters

α_2	[–]	empirical value
β	[–]	swarm packing correction

β_2	[–]	empirical value
δ	[m]	displacement
ε	[–]	porosity
η	[–]	damping coefficient
κ_N	[–]	Newton drag correction
κ_S	[–]	Stoke drag correction
μ	[–]	sliding friction coefficient
ρ	[$kg\,m^{-3}$]	density
τ	[$N\,m^{-2}$]	stress tensor
Φ	[–]	sphericity
$\Phi_\perp$	[–]	ratio between the cross-sectional area of the volume equivalent sphere and the projected cross-sectional area
$\Phi_\parallel$	[–]	ratio between the cross-sectional area of the volume equivalent sphere and the difference between half the surface area
Ψ	[–]	particle shape factor
$\Psi_\perp$	[m^2]	stream perpendicular particle projected area
$\Psi_\parallel$	[m^2]	stream wise particle projected area
ω	[s^{-1}]	angular velocity

Sub- and Superscripts

C	contact
D	drag
eq	equivalent volume
g	gas
i,j	*i*-th and *j*-th particle
n	normal
p	particle/particulate phase
t	tangential
r	rolling friction
σ	angle of inflow

Abbreviations

FBRG	fluidized bed rotor granulator
SQ	superquadric

References

[1] D. Weis, M. Evers, M. Thommes, S. Antonyuk, *Chem. Eng. Sci.* **2018**, *192 (3)*, 803–815. DOI: https://doi.org/10.1016/j.ces.2018.07.057

[2] *Granulation*, 1st ed. (Eds: S. M. Hounslow, J. P. K. Seville), Handbook of Powder Technology, Vol. 11, Elsevier, Amsterdam **2007**.

[3] S. Muley, T. Nandgude, S. Poddar, *Asian J. Pharm. Sci.* **2016**, *11 (6)*, 684–699. DOI: https://doi.org/10.1016/j.ajps.2016.08.001

[4] P. Grohn, D. Weis, M. Thommes, S. Heinrich, S. Antonyuk, *Chem. Eng. Technol.* **2020**, *43 (5)*, 887–895. DOI: https://doi.org/10.1002/ceat.201900517

[5] P. Grohn, M. Lawall, T. Oesau, S. Heinrich, S. Antonyuk, *Processes* **2020**, *8 (9)*, 1090. DOI: https://doi.org/10.3390/pr8091090

[6] A. Atxutegi, P. Kieckhefen, S. Pietsch, R. Aguado, M. Olazar, S. Heinrich, *Powder Technol.* **2021**, *389 (1)*, 493–506. DOI: https://doi.org/10.1016/j.powtec.2021.05.012

[7] N. G. Deen, M. van Sint Annaland, M. A. van der Hoef, J. A. M. Kuipers, *Chem. Eng. Sci.* **2007**, *62 (1–2)*, 28–44. DOI: https://doi.org/10.1016/j.ces.2006.08.014

[8] V. Salikov, S. Antonyuk, S. Heinrich, V. S. Sutkar, N. G. Deen, J. A. M. Kuipers, *Powder Technol.* **2015**, *270*, 622–636. DOI: https://doi.org/10.1016/j.powtec.2014.05.026

[9] P. Breuninger, D. Weis, I. Behrendt, P. Grohn, F. Krull, S. Antonyuk, *Particuology* **2019**, *42 (8)*, 114–125. DOI: https://doi.org/10.1016/j.partic.2018.03.015

[10] L. Fries, M. Dosta, S. Antonyuk, S. Heinrich, S. Palzer, *Chem. Eng. Technol.* **2011**, *34 (7)*, 1076–1084. DOI: https://doi.org/10.1002/ceat.201100132

[11] V. Salikov, S. Heinrich, S. Antonyuk, V. S. Sutkar, N. G. Deen, J. A. M. Kuipers, *Advanced Powder Technol.* **2015**, *26 (3)*, 718–733. DOI: https://doi.org/10.1016/j.apt.2015.02.011

[12] V. S. Sutkar, N. G. Deen, V. Salikov, S. Antonyuk, S. Heinrich, J. A. M. Kuipers, *Powder Technol.* **2015**, *270*, 537–547. DOI: https://doi.org/10.1016/j.powtec.2013.11.030

[13] D. Weis, P. Grohn, M. Evers, M. Thommes, E. García, S. Antonyuk, *Powder Technol.* **2021**, *378*, 667–679. DOI: https://doi.org/10.1016/j.powtec.2020.09.013

[14] T. Pöschel, T. Schwager, *Computational Granular Dynamics: Models and Algorithms*, 1st ed., Springer, Berlin **2010**.

[15] Y. Muguruma, T. Tanaka, Y. Tsuji, *Powder Technol.* **2000**, *109 (1–3)*, 49–57. DOI: https://doi.org/10.1016/S0032-5910(99)00226-0

[16] J. Neuwirth, *Charakterisierung und Diskrete-Partikel-Modellierung des Strömungs- und Dispersionsverhaltens im Rotorgranulator*, 1st ed., SPE-Schriftenreihe, Vol. 7, Cuvillier Verlag, Göttingen **2017**.

[17] Y. He, F. Muller, A. Hassanpour, A. E. Bayly, *Chem. Eng. Sci.* **2020**, *223 (10)*, 115712. DOI: https://doi.org/10.1016/j.ces.2020.115712

[18] M. Pasha, C. Hare, M. Ghadiri, A. Gunadi, P. M. Piccione, *Powder Technol.* **2016**, *296 (1)*, 29–36. DOI: https://doi.org/10.1016/j.powtec.2015.10.055

[19] N. Govender, D. N. Wilke, C.-Y. Wu, R. Rajamani, J. Khinast, B. J. Glasser, *Adv. Powder Technol.* **2018**, *29 (10)*, 2476–2490. DOI: https://doi.org/10.1016/j.apt.2018.06.028

[20] W. Zhong, A. Yu, X. Liu, Z. Tong, H. Zhang, *Powder Technol.* **2016**, *302*, 108–152. DOI: https://doi.org/10.1016/j.powtec.2016.07.010

[21] J. F. Favier, M. H. Abbaspour-Fard, M. Kremmer, A. O. Raji, *Eng. Comput.* **1999**, *16 (4)*, 467–480. DOI: https://doi.org/10.1108/02644409910271894

[22] R. Hesse, F. Krull, S. Antonyuk, *Powder Technol.* **2021**, *393*, 559–581. DOI: https://doi.org/10.1016/j.powtec.2021.07.056

[23] B. Soltanbeigi, A. Podlozhnyuk, S.-A. Papanicolopulos, C. Kloss, S. Pirker, J. Y. Ooi, *Powder Technol.* **2018**, *329 (1)*, 288–303. DOI: https://doi.org/10.1016/j.powtec.2018.01.082

[24] S. Antonyuk, *Particles in Contact*, Springer International, Cham **2019**.

[25] P. Grohn, D. Weis, U. Bröckel, S. Heinrich, S. Antonyuk, in *Particles in Contact*, Vol. 12 (Eds: S. Antonyuk), Springer International, Cham **2019**.

[26] H. Kruggel-Emden, S. Rickelt, S. Wirtz, V. Scherer, *Powder Technol.* **2008**, *188 (2)*, 153–165. DOI: https://doi.org/10.1016/j.powtec.2008.04.037

[27] D. Weis, *Beschreibung des Sphäronisationsprozesses von pharmazeutischen Pellets mittels numerischer Methoden*, Dissertation, Technische Universität Kaiserslautern **2020**.

[28] A. H. Barr, *IEEE Comput. Grap. Appl.* **1981**, *1 (1)*, 11–23. DOI: https://doi.org/10.1109/MCG.1981.1673799
[29] P. W. Cleary, *Powder Technol.* **2013**, *248 (6)*, 103–120. DOI: https://doi.org/10.1016/j.powtec.2013.06.010
[30] H. Ma, Y. Zhao, *Chem. Eng. Sci.* **2017**, *172*, 636–651. DOI: https://doi.org/10.1016/j.ces.2017.07.017
[31] H. Ma, Y. Zhao, *Granular Matter* **2018**, *20 (3)*, 47. DOI: https://doi.org/10.1007/s10035-018-0823-0
[32] S. Ji, S. Wang, Z. Zhou, *Adv. Powder Technol.* **2020**, *31 (8)*, 3540–3550. DOI: https://doi.org/10.1016/j.apt.2020.06.040
[33] V. S. Sutkar, T. J. K. van Hunsel, N. G. Deen, V. Salikov, S. Antonyuk, S. Heinrich, J. A. M. Kuipers, *Chem. Eng. Sci.* **2013**, *102*, 524–543. DOI: https://doi.org/10.1016/j.ces.2013.08.046
[34] S. K. P. Sanjeevi, J. A. M. Kuipers, J. T. Padding, *Int. J. Multiphase Flow* **2018**, *106 (1)*, 325–337. DOI: https://doi.org/10.1016/j.ijmultiphaseflow.2018.05.011
[35] X. Gao, J. Yu, L. Lu, C. Li, W. A. Rogers, *Chem. Eng. J.* **2021**, *420*, 127654. DOI: https://doi.org/10.1016/j.cej.2020.127654
[36] A. Hölzer, M. Sommerfeld, *Powder Technol.* **2008**, *184 (3)*, 361–365. DOI: https://doi.org/10.1016/j.powtec.2007.08.021
[37] J. H. Ferziger, M. Perić, *Computational Methods for Fluid Dynamics*, Springer, Berlin **2002**.
[38] P. A. Cundall, O. D. L. Strack, *Géotechnique* **1979**, *29 (1)*, 47–65. DOI: https://doi.org/10.1680/geot.1979.29.1.47
[39] C. Kloss, C. Goniva, A. Hager, S. Amberger, S. Pirker, *Prog. Comput. Fluid Dyn.* **2012**, *12 (2–3)*, 140. DOI: https://doi.org/10.1504/PCFD.2012.047457
[40] A. Podlozhnyuk, S. Pirker, C. Kloss, *Comp. Part. Mech.* **2017**, *4 (1)*, 101–118. DOI: https://doi.org/10.1007/s40571-016-0131-6
[41] J. R. Williams, A. P. Pentland, *Eng. Comput.* **1992**, *9 (2)*, 115–127. DOI: https://doi.org/10.1108/eb023852
[42] J. Verbeke, R. Cools, *Int. J. Math. Educ. Sci. Technol.* **1995**, *26 (2)*, 177–193. DOI: https://doi.org/10.1080/0020739950260202
[43] Y. Tsuji, T. Tanaka, T. Ishida, *Powder Technol.* **1992**, *71 (3)*, 239–250. DOI: https://doi.org/10.1016/0032-5910(92)88030-L
[44] R. Goldman, *Comput. Aided Geom. Des.* **2005**, *22 (7)*, 632–658. DOI: https://doi.org/10.1016/j.cagd.2005.06.005
[45] R. Di Felice, *Int. J. Multiphase Flow* **1994**, *20 (1)*, 153–159. DOI: https://doi.org/10.1016/0301-9322(94)90011-6
[46] G. Bagheri, C. Bonadonna, *Powder Technol.* **2019**, *349*, 108. DOI: https://doi.org/10.1016/j.powtec.2018.12.040
[47] F. Dioguardi, D. Mele, P. Dellino, *J. Geophys. Res. Solid Earth* **2018**, *123 (1)*, 144–156. DOI: https://doi.org/10.1002/2017JB014926
[48] M. Zastawny, G. Mallouppas, F. Zhao, B. van Wachem, *Int. J. Multiphase Flow* **2012**, *39*, 227–239. DOI: https://doi.org/10.1016/j.ijmultiphaseflow.2011.09.004
[49] B. E. Launder, D. B. Spalding, *Comput. Methods Appl. Mech. Eng.* **1974**, *3 (2)*, 269–289. DOI: https://doi.org/10.1016/0045-7825(74)90029-2
[50] C. Y. Wen, Y. H. Yu, *Chem. Eng. Prog. Symp. Ser.* **1966**, *62*, 100–111.
[51] R. Hesse, F. Krull, S. Antonyuk, *Powder Technol.* **2020**, *372*, 404–419. DOI: https://doi.org/10.1016/j.powtec.2020.05.113
[52] T. Oesau, P. Grohn, S. Pietsch-Braune, S. Antonyuk, S. Heinrich, *Adv. Powder Technol.* **2022**, *33 (1)*, 103362. DOI: https://doi.org/10.1016/j.apt.2021.11.014
[53] P. Grohn, T. Oesau, S. Heinrich, S. Antonyuk, *Powder Technol.* **2022**, *408*, 117736. DOI: https://doi.org/10.1016/j.powtec.2022.117736

